Chinese Chemical Letters 34 (2023) 107949

Contents lists available at ScienceDirect

Chinese Chemical Letters

journal homepage: www.elsevier.com/locate/cclet

Facile synthesis of ultrabright luminogens with specific lipid droplets targeting feature for *in vivo* two-photon fluorescence retina imaging

Huifang Su[a,1,*], Tao Xie[d,1], Yong U. Liu[d], Yuhan Cui[e], Wei Wen[a], Ben Zhong Tang[c,*], Wei Qin[b,*]

[a] Department of Orthopaedic Surgery, The First Affiliated Hospital of Zhengzhou University, Zhengzhou 450052, China
[b] Medical Research Center, Guangdong Provincial People's Hospital, Guangdong Academy of Medical Sciences, Guangzhou 510080, China
[c] School of Science and Engineering, Shenzhen Institute of Aggregate Science and Technology, The Chinese University of Hong Kong, Shenzhen 518172, China
[d] Laboratory for Neuroscience in Health and Disease, Guangzhou First People's Hospital, School of Medicine, South China University of Technology, Guangzhou 510180, China
[e] School of Materials Science and Engineering, Sun Yat-sen University, Guangzhou 510275, China

ARTICLE INFO

Article history:
Received 1 September 2022
Revised 17 October 2022
Accepted 23 October 2022
Available online 1 November 2022

Keywords:
Fluorescent probe
Lipid droplets (LDs)
Two-photon fluorescence (2PF) imaging
Retina imaging

ABSTRACT

The application of fluorescent probes for *in vivo* retinal imaging is of great importance, which could provide direct and crucial imaging evidence for a better understanding of common eye diseases. Herein, a group of bright organic luminogens with typical electron-donating (D) and electron-accepting (A) structures (abbreviated as LDs-BDM, LDs-BTM, and LDs-BHM) was synthesized through a simple single-step reaction. They were found to be efficient solid-state emitters with high fluorescence quantum yields of above 70% (*e.g.*, 83.7% for LDs-BTM). Their light-emission properties could be tuned by the modulation of π-conjugation effect with methoxy groups at different substituent positions. Their resulting fluorescent nanoparticles (NPs) were demonstrated as specific lipid droplets (LDs) targeting probes with high brightness, good biocompatibility, and satisfactory photostability. LDs-BTM NPs with a large two-photon absorption cross section ($\sigma_2 = 249$ GM) were further utilized as ultrabright two-photon fluorescence (2PF) nanoprobes for *in vivo* retina imaging of live zebrafish by NIR excitation at an ultralow concentration (0.5 μmol/L). Integrated histological structures at the tissue level and corresponding fine details at the cellular level of the embryonic retina of live zebrafish were clearly demonstrated. This is the first report of using ultrabright LDs-targeting nanoprobes to accurately measure fine details in the retina with 2PF microscopic technique. These good results are anticipated to open up a new avenue in the development of efficient 2PF emitters for non-invasive bioimaging of living animals.

Lipid droplets (LDs) are the monolayer of amphipathic lipids-covered organelles in most cells and organisms [1], which mainly include phospholipids, diacylglycerol, cholesterol, and sphingomyelin [2]. They are normally involved in multiple cellular functions, such as lipid metabolism, signal transduction, as well as protein degradation. Besides normal cell physiological functions [3], LDs are strongly associated with a series of lipid imbalance diseases, such as obesity, cancer, cardiovascular disease, and fatty liver disease [4]. Thus, LDs are important tools and can provide crucial information on the complex cascade of cellular events and molecular mechanisms.

To study significant biological functions and intrinsic mechanisms of LDs for biomedical applications, extensive research has been conducted based on conventional imaging techniques, such as Raman microscopy and transmission electron microscopy [5,6]. However, these imaging methods normally require complicated and time-consuming operation procedures, which still fail in real-time detection and *in vivo* monitoring of biological samples. Therefore, the development of simple and effective imaging methods for *in situ* visualization and monitoring of LDs in living cells and animals is of great importance.

Fluorescence imaging is a widely used imaging technique with high sensitivity, which enables non-invasive imaging of cell microenvironment *in vitro* and complicated biological processes *in vivo* [7–16]. Sphingolipids, as one type of LDs species, are abundant in animal retinal lipids [17,18]. They play an essential role in the development and realization of the visual function of the

* Corresponding authors.
E-mail addresses: suhuif@mail2.sysu.edu.cn (H. Su), tangbenz@cuhk.edu.cn (B.Z. Tang), qinwei@gdph.org.cn (W. Qin).
[1] These authors contributed equally to this work.

https://doi.org/10.1016/j.cclet.2022.107949
1001-8417/

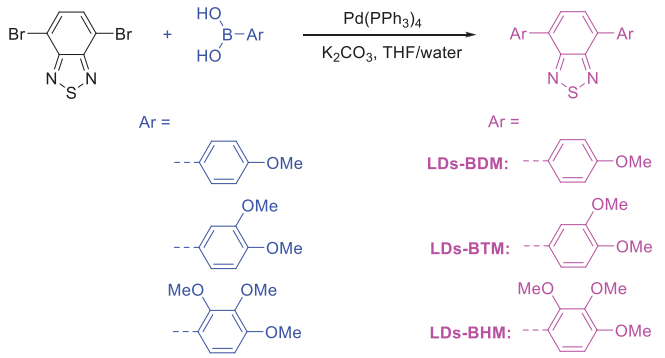

Fig. 1. The synthetic pathway and chemical structures of LDs-BDM, LDs-BTM and LDs-BHM.

retina and are closely related to the pathogenesis of ocular diseases as well [19,20]. Unfortunately, there are few reports of fluorescent materials with specific LDs-targeting features for retinal imaging [21–24]. Thus, the application of fluorescent probes for retinal imaging *in vivo* is of great importance as it can provide direct imaging evidence for understanding common eye disorders and diseases, such as diabetic retinopathy [25].

Two-photon fluorescence (2PF) imaging is an indispensable technique for *in vivo* imaging due to its near-infrared (NIR) excitation, high spatial resolution, and signal-to-background ratio (SBR) [26,27]. Nevertheless, many organic fluorescent chromophores suffer from low two-photon absorption (2PA) cross sections (σ_2 < 50 GM, 1 GM = 1×10^{-50} cm^4 s $photon^{-1}$ $molecule^{-1}$) or from short wavelength emissions [28,29]. To improve the two-photon absorption of chromophores, scientists have designed various organic fluorescent materials based on strong electron-donating (D) and electron-accepting (A) systems [30,31]. To achieve efficient light-emission properties and outstanding imaging performance of materials, researchers have made significant progress in developing organic fluorescent materials with aggregation-induced emission (AIE) features [32–41]. Unfortunately, some AIE functional materials are involved in multistep organic synthesis and a time-consuming separation process [42–44], which inevitably hinders their practical bioimaging applications.

With this background in mind, a series of bright luminogens (namely LDs-BDM, LDs-BTM, and LDs-BHM) was designed and synthesized herein by a one-step Suzuki coupling with satisfactory yield. These molecules (Fig. 1) constructed from 2,1,3-benzothiadiazole [45,46] core and anisole moieties were found to be ultrabright emitters with high quantum efficiencies (*e.g.*, 83.7% for LDs-BTM) in the solid state. Their fluorescence properties could be regulated by the modulation of π-conjugation effect with methoxy groups at *meta* and *ortho* positions. Their corresponding nanoparticles (NPs) exhibited high brightness, specific LDs-targeting property, satisfactory biocompatibility, and good photostability. To explore new bioimaging applications, LDs-BTM NPs with a large σ_2 value of 249 GM were further utilized as ultrabright fluorescent nanoprobes for high-contrast 2PF imaging of the embryonic retina of live zebrafish *in vivo*. Highly emissive LDs-targeting nanoprobes were employed for the accurate measurement of fine details of the retina with 2PF microscopic technique for the first time herein. Therefore, this work is expected to inspire new research interests in the development of efficient 2PF materials for the clinical studies of common ocular disorders and diseases.

The reported organic luminogens (abbreviated as LDs-BDM, LDs-BTM, and LDs-BHM) were constructed from 2,1,3-benzothiadiazole unit and anisole groups (Fig. 1). Based on the *para*-substituted molecular skeleton of LDs-BDM, its structural adducts (*e.g.*, LDs-BTM and LDs-BHM) with more methoxy groups at *meta* and *ortho* positions were designed (Fig. 1). Consequently, their absorption and emission color could be tuned by structural optimization. The three organic dyes were simply synthesized through a single-step reaction from inexpensive commercial products with satisfactory yields. Their chemical structures were fully characterized by high-resolution mass spectrometry (HRMS), nuclear magnetic resonance (NMR), and single-crystal X-ray diffraction analysis (XRD). The characterization results were given in Figs. S1-S9 (Supporting information).

All three luminogens showed good solubility in common organic solvents, such as toluene (TOL), dichloromethane (DCM), tetrahydrofuran (THF), *N*,*N*-dimethylformamide (DMF), and dimethyl sulfoxide (DMSO), but were found to be insoluble in water. Absorption spectra of LDs-BDM, LDs-BTM and LDs-BHM in THF showed peaks at 414, 425 and 389 nm, respectively, which were changed slightly by solvent polarity (Figs. S10-S12 in Supporting information). Their photoluminescence (PL) spectra in solvents with different polarities were also investigated (Figs. S10-S12). When the solvent polarity was increased from nonpolar TOL to highly polar DMSO, the emission maxima of LDs-BDM, LDs-BTM, and LDs-BHM were red-shifted from 527 nm to 563 nm, 549 nm to 588 nm, and 510 nm to 541 nm, respectively. This phenomenon suggested positive solvatochromism due to the intramolecular charge transfer (ICT) effect [45]. Notably, quantum efficiencies of LDs-BDM, LDs-BTM and LDs-BHM in solid films were measured to be 87.8%, 83.7% and 74.3% (Table S1 in Supporting information), respectively, which are favorable for high-contrast bioimaging applications. The lifetimes of LDs-BDM, LDs-BTM and LDs-BHM in the solid-powder state were measured to be 8.1, 18.8 and 7.8 ns (Table S1), respectively, revealing the fluorescence nature of the light emission rather than long-lived delayed fluorescence or phosphorescence (Fig. S13 in Supporting information).

To obtain further insight into the effect of molecular structures on fluorescent emission of LDs-BDM, LDs-BTM, and LDs-BHM, their single-crystals were grown and analyzed by X-ray diffraction. The crystal data and the related parameters are shown in Figs. S14-S16 and Tables S2-S4 (Supporting information). As seen from the crystal structures in Fig. 2, LDs-BTM adopted a nearly planar conformation with small dihedral angles of 3.32° and 3.73° between the 2,1,3-benzothiadiazole moiety (P_1) and the adjacent phenyl rings (P_2 and P_3). Small torsion angles between methoxy groups and adjacent benzene rings were also calculated to be 5.53°, 7.96°, 10.68°, and 10.96°, respectively. Such a nearly planar conformation of LDs-BTM molecule favors π-electron conjugation and delocalization. LDs-BTM was packed in the monoclinic space group C2/c, from which two representative dimers were extracted to study the molecular packing. Multiple C-H···π interactions were present in adjacent molecules with short bond lengths (*e.g.*, 2.858, 2.958, and 3.002 Å in dimer **1**). It is noteworthy that in LDs-BTM crystals, the hydrogen atoms of benzene rings and methoxy groups participated in intermolecular hydrogen bonding interactions. For example, multiple C-H···N and C-H···O interactions existed in crystals with short hydrogen bonding distances (*e.g.*, 2.931 and 2.939 Å in dimer **1**, and 2.765, 3.055 and 3.062 Å in dimer **2**). These multiple interactions between adjacent molecules in LDs-BTM crystals greatly restricted the molecular motions and efficiently suppressed the loss of excited-state energy through nonradiative decay channels, enabling the molecules to emit intense fluorescence in crystals. Different from LDs-BTM, LDs-BHM adopted a twisted conformation in the crystal state (Fig. 2). The dihedral angles between P_1 and adjacent P_2 and P_3 were measured to be 46.67° and 48.62°, respectively, which were much larger than those of LDs-BTM (3.32° and 3.73°), leading to a remarkable molecular nonplanarity. In contrast, LDs-BDM was in between LDs-BTM and LDs-

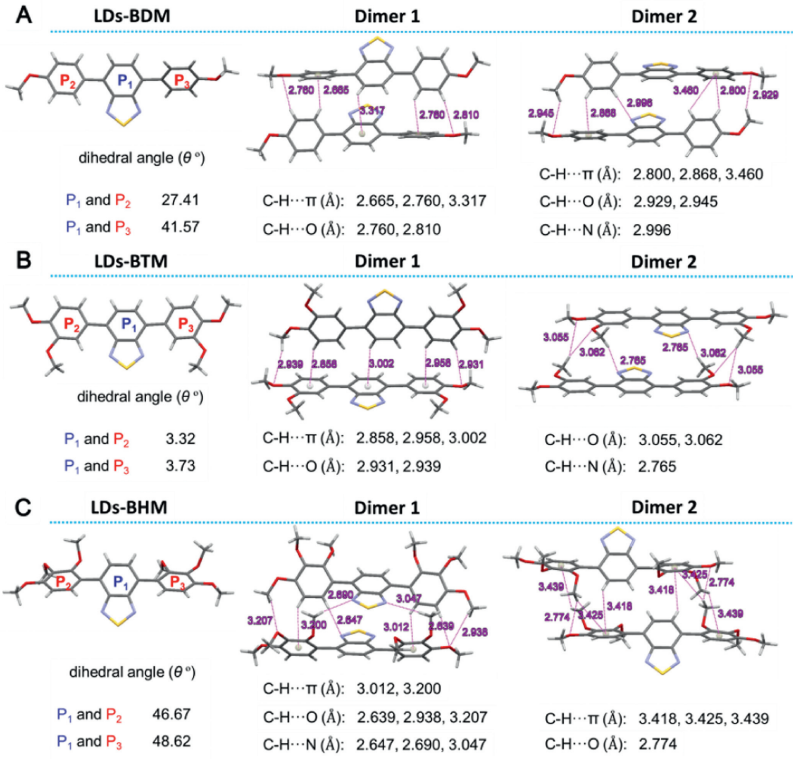

Fig. 2. Crystal structures and representative dimers of (A) LDs-BDM, (B) LDs-BTM, and (C) LDs-BHM with bond lengths.

BHM in terms of dihedral angles (27.41° and 41.57°) and molecular non-planarity. LDs-BDM and LDs-BHM crystallized in the monoclinic space group $P2_1/n$, from which the corresponding representative dimers were extracted. Abundant C-H···N, C-H···O, and C-H···π interactions also existed in the crystal lattice (Figs. 2A and C). Therefore, the introduction of methoxy groups at *meta* and *ortho* positions led to significant changes in molecular conformation, electron conjugation, and crystal packing. Such a successful structural optimization favors the absorption and emission tuning of luminogens.

For a better understanding of the electronic distributions of LDs-BTM, LDs-BDM and LDs-BHM at the molecular level, density functional theory calculations were performed (Fig. S17 in Supporting information). The three molecules demonstrated a similar electronic distribution. For example, the electron clouds of the highest occupied molecular orbital (HOMO) of LDs-BDM were dispersed on the whole molecule except methyl groups. In contrast, the lowest unoccupied molecular orbital (LUMO) of LDs-BDM was mainly concentrated on orbitals of the P_1 core. The difference in electron distribution of HOMO and LUMO between LDs-BTM, LDs-BDM, and LDs-BHM indicated an intrinsic ICT feature, which is consistent with the experimental phenomenon of positive solvatochromism shown in Figs. S10-S12.

The bright emission of LDs-BDM, LDs-BTM and LDs-BHM with high fluorescence yields in the solid state prompted an investigation of their bioimaging applications [47]. Although they were insoluble in water, their resultant NPs could be simply fabricated by nanoprecipitation. The sizes of their corresponding NPs in aqueous solutions were measured by dynamic light scattering (DLS). The corresponding hydrodynamic diameters were measured to be 104, 119 and 105 nm, respectively (Fig. S18 in Supporting information). LDs-BDM, LDs-BTM, and LDs-BHM NPs emitted intense fluorescence with high quantum efficiencies of 47.4%, 56.2% and 64.1%, respectively, making them promising candidates for high-contrast *in vitro* and *in vivo* bioimaging applications.

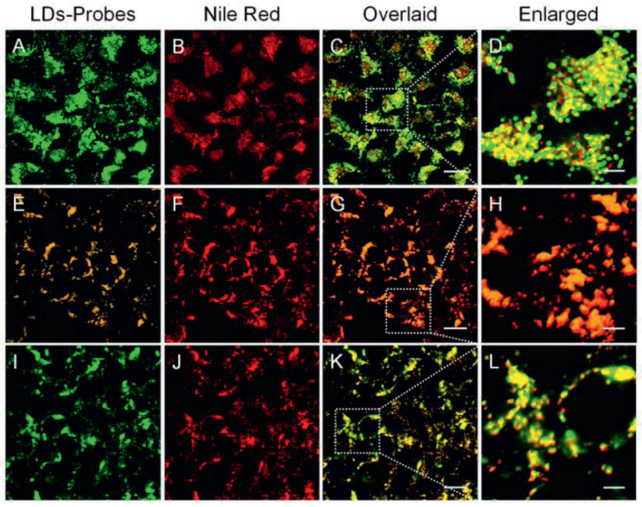

Fig. 3. (A-L) Confocal laser scanning microscopic images of HeLa cells incubated with different LDs-probes (A: LDs-BDM, E: LDs-BTM, and I: LDs-BHM) (0.5 μmol/L), and Nile Red (100 μg/mL). Scale bar: 20 μm (A-C, E-G, and I-K); 5 μm (D, H and L).

In vitro cell imaging was conducted using confocal laser scanning microscopy. After incubation of HeLa cells with the nanoprobes of LDs-BDM, LDs-BTM, and LDs-BHM for 40 min, intense fluorescence in the cytoplasm was observed using the lowest excitation power (405 nm, 0.2% power) at the ultralow working concentration of 20 nmol/L (Fig. S19 in Supporting information). The result is indicative of their high brightness and satisfactory cell permeability. To further confirm the intracellular location in live cells, co-staining tests with a commercial lipid droplet dye (namely Nile red) were carried out. As shown in Fig. 3, LDs-BDM, LDs-BTM and LDs-BHM molecules were distributed in HeLa cells similar to Nile Red. The corresponding co-staining colocalization coefficients

(Manders) with Nile Red are as high as 0.91, 0.97, and 0.92, respectively. Evidently, LDs-BDM, LDs-BTM and LDs-BHM demonstrate a specific LDs-targeting feature [48–50].

Normally, the native microenvironment of lipid droplets in cells is lipophilic, which contains plenty of hydrophobic ingredients, such as phospholipids, diacylglycerol, cholesterol and sphingomyelin [2]. The relatively high hydrophobicity of organic molecules favors the specific LDs targeting owing to the law of similarity and intermiscibility. For a better understanding of the high specificity of LDs-BDM, LDs-BTM and LDs-BHM for LDs, theoretical calculations were carried out using ChemBioDraw 14.0. Generally, the aqueous solubility of a small molecule depends on its hydrophobicity or log*P* (*n*-octanol/water partition coefficient) value. Here, ClogP was defined as the calculated log*P* [51], and the Clog*P* values of LDs-BDM, LDs-BTM and LDs-BHM were estimated to be 5.59, 5.07, and 3.23, respectively. These values were close to Clog*P* values of commercial LDs dyes (Lipid Green: 4.07, Nile Red: 4.618, and BODIPY 493/503: 5.028) and other previously reported LDs probes (SF44: 5.501 and LD 540: 5.996) [52,53], which probably explains the typical LDs-targeting property of the three LDs probes.

Then, the cytotoxicity of the LDs-targeting probes was evaluated by measuring the metabolic viability of HeLa cells after incubation at different dye concentrations (0.5, 1, 2, 5 and 10 μmol/L). The cell viability was above 95% after incubation with HeLa cells for 24 h (Fig. S20A in Supporting information), indicating the low cytotoxicity of the nanoprobes at the tested concentrations. As photostability is one of the essential prerequisites for bioimaging applications, the PL intensity was investigated at different time points. Fig. S20B (Supporting information) illustrates the fluorescence changes of new LDs probes and commercial BODIPY 493/503 dye in cells upon irradiation at 405 nm after 40 laser scans. All three LDs probes showed stable fluorescence signals and retained >94% of their initial fluorescence intensity after laser irradiation at the same working concentration. In contrast, only 66% of the initial fluorescence was maintained in BODIPY 493/503 dye. Thus, LDs-BDM, LDs-BTM and LDs-BHM demonstrated high brightness, outstanding LDs-targeting property, low cytotoxicity, and satisfactory photostability, which were promising candidates for further *in vivo* bioimaging applications.

2PF is a typical photophysical process, which is illustrated in Fig. S21A (Supporting information). A molecule is excited from the singlet ground state (S_0) to the nth excited singlet state (S_n) by simultaneous absorption of two lower-energy photons. After the excitation process, the fluorophore decays to the lowest energy level of the first excited singlet state (S_1) *via* non-radiative transitions, followed by the same radiative decay pathway as that of one-photon process [54]. Compared to LDs-BDM and LDs-BHM, LDs-BTM emits longer wavelength fluorescence at the same experimental conditions, which is one of the promising candidates for high-contrast fluorescence imaging. A preliminary study of two-photon absorption property of LDs-BTM NPs in water was conducted at different excitation wavelengths from 800 nm to 900 nm (Fig. S21B in Supporting information). The LDs-BTM aggregates exhibited a strong two-photon absorption peak with the maximum value of 249 GM under 850 nm laser excitation. The two-photon absorption cross section (σ_2) value of LDs-BTM NPs was higher than that of traditional dyes, such as fluorescent proteins (*e.g.* 39 GM for EGFP), BODIPY dyes and other organic fluorescent materials [28,55,56]. Besides the maximum excitation at 850 nm, LDs-BTM NPs could also be excited at the nearby wavelengths of 820, 840, and 860 nm for two-photon LD imaging in live cells at low concentrations of 0.25, 0.5, and 1.0 μmol/L (Fig. S22 in Supporting information), which shows great potential for *in vivo* 2PF imaging.

Zebrafish is a widely used vertebrate model organism, whose 99% of embryonic essential genes are conserved in humans [57]. It was selected as the animal model for *in vivo* 2PF imaging of LDs due to its optical transparency, small size as well as easy availability [58,59]. As illustrated in Figs. S23A and S24 (Supporting information), intense red fluorescence signals were observed from the yolk sac of zebrafish at 2–4 days post-fertilization (dpf) after staining with LDs-BTM NPs (0.25 μmol/L) for 2 h. The three-dimensional (3D) image from the imaging view direction reveals the shape and depth information of zebrafish (Fig. S23B in Supporting information). The yolk sac is an important organ of zebrafish mainly indicated by red color, which stores neutral lipids and polar phospholipids, and supplies nutrients and energy for the growth of zebrafish [60]. It is noteworthy that a partial fluorescence signal was also observed from the eyeball of zebrafish under the same experimental conditions. The same conclusion was drawn from the semi-quantitative analysis of the region of interest (ROI) in fluorescence images in Fig. S23C (Supporting information). When the dye concentration of 0.25 μmol/L was utilized for staining, the average gray values of the yolk sac and eyeballs were calculated to be 79.8 and 50.3, which were much higher than those of the spinal cord (25.9), the otic capsule (21.2) and the notochord (6.9). Therefore, the fluorescent LDs-BTM NPs were mainly enriched in the yolk sac and partly accumulated in eyeballs as well.

As retinal neurogenesis of zebrafish eyes is mostly completed at 3 dpf [61], 2PF microscopic scanning at different depths was utilized to obtain integrated details of the embryonic retina. The lens was used as a reference for a better understanding of the anatomy of the eyeball. Along the long axis (z-axis) of the lens, four representative images of the zebrafish eyeball were obtained (Figs. 4A-D), which revealed the delicate structures of the embryonic retina viewed from different directions at various depths from 36 μm to 108 μm. Other 2PF images of the embryonic retina at depths from 28 μm to 124 μm were shown in Fig. S25 (Supporting information). The signal to background ratios (SBRs) of the 2PF images at depths of 20, 40, 60, 80, 100, and 120 μm were calculated to be 159.8, 146.6, 139.5, 64.6, 43.6, and 34.3, respectively (Fig. 4E). The high SBR could be attributed to the remarkable nonlinear optical effect, the high penetration depth of the NIR excitation, and the strong 2PF signal of the LDs-BTM NPs. The gradual 2PF signal loss was attributed to the light absorption and scattering by the tissue of the zebrafish eye. Fig. 4F presented a high-contrast representative 2PF image at the penetration depth of 80 μm, which demonstrated an integrated picture of the embryonic retina, including the sophisticated histological structures and the fine details of staggered network-like structures. From the center of the eyeball to the periphery, the fine structures of lens (*le*), ganglion cell layer (*gcl*), inner plexiform layer (*ipl*), inner nuclear layer (*inl*), outer plexiform layer (*opl*), outer plexiform layer (*onl*), and pigmented epithelium (*pe*) could be clearly differentiated [62]. Evidently, LDs-BTM probe exhibited outstanding retina labeling capability *in vivo*, different from commercial lipophilic tracers (*e.g.* DiI, DiO) used for ganglion cell labeling *in vitro* [63–65]. After careful measurement of the high-contrast image, abundant quantitative information was obtained. The lens was spherical with a radius (*r*) of 52.4 μm. The *gcl* of the embryonic retina was composed of ganglion cells, while *inl* was mainly constructed from the cell bodies of horizontal cells, bipolar cells, amacrine cells, interplexiform neurons, and Müller cells. The different cellular species in *gcl* and *inl* of the retina could be easily differentiated by their different average sizes. For example, the average cell size in the selected ROI in *gcl* (marked as area a) was measured to be 40.89 μm^2, while the average cell size in the ROI in *inl* (labeled as area b) was measured to be 16.04 μm^2, which is consistent with previous reports [62]. The average thicknesses of *opl* and *pe* were measured to be 6.5 and 11.1 μm, respectively. Fig. 4G shows the full width at half maximum (FWHM) of the indicated tiny structure (dotted line c) in Fig. 4F, which was calculated to be 2.36 μm. Therefore, based on

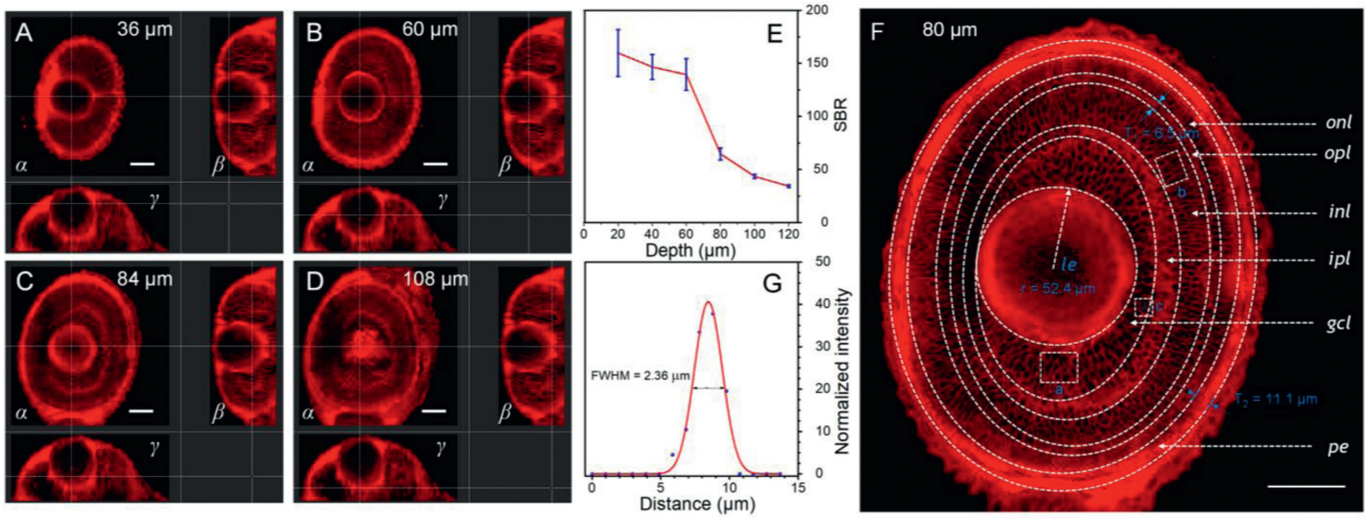

Fig. 4. (A-D) 2PF images of embryonic retina of zebrafish at 3 dpf in (A) anterior 1/4, (B) middle 1/2, (C) posterior 1/4, and at (D) the bottom of the lens. Viewing from different directions: α) x–y plane; β) x–z plane; γ) y–z plane. Scale bar: 50 μm. (E) Attenuation curve of the 2PF signal. (F) Representative 2PF histology image of embryonic retina of zebrafish. Areas a and b are the ROIs of *gcl* and *inl*, respectively. Scale bar: 50 μm. (G) A cross-sectional intensity profile measured along the blue dotted line c in (F).

the efficient 2PF LDs-targeting nanoprobes, integrated histological structures at the tissue level and corresponding fine details at the cellular level of the embryonic retina of live zebrafish were clearly distinguished. In recent years, numerous luminogens have been reported for LDs imaging with different bioimaging applications [66–71]. These fluorescent materials are synthesized by multistep reactions with complicated chemical structures, while the present molecule (namely LDs-BTM) can be facilely prepared through a one-step reaction with a simple chemical structure and specific LDs targeting feature. Some previous works are hampered by the intrinsic optical properties of fluorescent materials with low solid-state fluorescence quantum yields (<15%) and/or short one-photon excitation wavelengths in the visible region [72–77]. In contrast, LDs-BTM has a high fluorescence quantum efficiency and long two-photon excitation wavelengths in NIR region. Furthermore, different from commercial labeling agents BODIPY-ceramides with long incubation periods (normally 2–8 h) at high concentrations (*ca.* 50–100 μmol/L) [24,78], LDs-BTM is a highly efficient LDs probe with outstanding 2PF property, which enables *in vivo* high-contrast retina imaging with a short incubation period (*e.g.*, 2 h) at a low concentration (*e.g.*, 0.5 μmol/L).

In summary, a series of organic luminogens (namely LDs-BDM, LDs-BTM, and LDs-BHM) constructed from 2,1,3-benzothiadiazole core and anisole moieties was designed and facilely synthesized. All three luminogens showed bright fluorescence in the solid state with high fluorescence quantum yields of above 70% (*e.g.*, 83.7% for LDs-BTM). The positions of methoxy group substituent of dyes significantly influenced their photophysical properties *via* π-conjugation effect. Their corresponding NPs exhibited high brightness, specific LDs-targeting feature, satisfactory biocompatibility, as well as good photostability. Ultrabright LDs-BTM NPs were further used as efficient 2PF nanoprobes for *in vivo* retina imaging of live zebrafish by NIR excitation at an ultralow concentration of 0.5 μmol/L. Integrated histological structures at the tissue level and corresponding fine details at the cellular level of the retina of live zebrafish were clearly differentiated. The accurate measurement of delicate structures in the embryonic retina with 2PF microscopic technique is first reported herein with ultrabright LD-specific nanoprobes. This work is expected to facilitate the development of efficient solid-state dyes with outstanding 2PF effect for non-invasive optical imaging of live animals.

Declaration of competing interest

The authors declare that they have no conflict of interest.

Acknowledgments

We gratefully acknowledge the National Natural Science Foundation of China (Nos. 81902356, 82072581, 21971265 and 82272842), Programs for Medical Science and Technology Research Project of Henan Province Health Commission (Nos. 2018020025, SB201901029), Henan Province Young and Middle-Aged Health Science and Technology Innovation Talent Project (No. YXKC2022032), Shenzhen Key Laboratory of Functional Aggregate Materials (No. ZDSYS20211021111400001) and Provincial Science and Technology R&D Program Joint Fund of the Department of Science and Technology of Henan Province (superior discipline cultivation category) Key Project (No. 222301420018). The authors are grateful to Prof. Zhiyong Yang from School of Chemistry in Sun Yat-sen University for the support of theoretical calculations. We thank the Translational Medical Center, First Affiliated Hospital of Zhengzhou University for technical support. The current study was approved by the Ethics Review Board of The First Affiliated Hospital of Zhengzhou University. All experimental activities were in accord with the 1964 Declaration of Helsinki.

Supplementary materials

Supplementary material associated with this article can be found, in the online version, at doi:10.1016/j.cclet.2022.107949.

References

[1] R.V. Farese, T.C. Walther, Cell 139 (2009) 855–860.
[2] R. Bartz, W.H. Li, B. Venables, et al., J. Lipid. Res. 48 (2007) 837–847.
[3] W.H. Fei, H. Wang, X. Fu, C. Bielby, H.Y. Yang, Biochem. J. 424 (2009) 61–67.
[4] P. Dalhaimer, Cells 8 (2019) 974.
[5] K. Majzner, K. Kochan, N. Kachamakova-Trojanowska, et al., Anal. Chem. 86 (2014) 6666–6674.
[6] S. Angermüller, H.D. Fahimi, Histochem. J. 14 (1982) 823–835.
[7] Z.L. Zeng, S.S. Liew, X. Wei, K.Y. Pu, Angew. Chem. Int. Ed. 60 (2021) 26454–26475.
[8] X. Zhang, Y. Chen, H.S. He, et al., Angew. Chem. Int. Ed. 60 (2021) 26337–26341.
[9] W. Qin, N. Alifu, J.W.Y. Lam, et al., Adv. Mater. 32 (2020) 2000364.

[10] H. Zhu, J.L. Fan, J.J. Du, X.J. Peng, Acc. Chem. Res. 49 (2016) 2115–2126.
[11] Y.H. Li, Y. Sun, J.C. Li, et al., J. Am. Chem. Soc. 137 (2015) 6407–6416.
[12] W. Qin, D. Ding, J.Z. Liu, et al., Adv. Funct. Mater. 22 (2012) 771–779.
[13] H.F. Su, Z.W. Deng, Y.L. Liu, et al., Mater. Chem. Front. 6 (2022) 1317–1323.
[14] H.Q. Cao, Y. Yang, J.B. Li, Aggregate 1 (2020) 69–79.
[15] J. Chen, W.J. Liu, X.N. Fang, Q.L. Qiao, Z.C. Xu, Chin. Chem. Lett. 33 (2022) 5042–5046.
[16] X. Shi, G. Gao, X.Y. Liu, et al., Chin. Chem. Lett. 34 (2023) 107613.
[17] R.S. Brush, J.T. Tran, K.R. Henry, et al., Invest. Ophthalmol. Vis. Sci. 51 (2010) 4422–4431.
[18] M.V. Simón, F.H. Prado Spalm, M.S. Vera, N.P. Rotstein, Front. Cell Neurosci. 13 (2019) 246.
[19] J.M. Harmon, D. Bacikova, K. Gable, et al., J. Biol. Chem. 288 (2013) 10144–10153.
[20] H. Chen, A.Y. Chan, D.U. Stone, N.A. Mandal, Surv. Ophthalmol. 59 (2014) 64–76.
[21] K. Watanabe, Y. Nishimura, T. Oka, et al., BMC Neurosci. 11 (2010) 116.
[22] S. Rieger, R.P. Kulkarni, D. Darcy, S.E. Fraser, R.W. Köster, Dev. Dyn. 234 (2005) 670–681.
[23] V.P. Connaughton, D. Graham, R. Nelson, J. Comp. Neurol. 477 (2004) 371–385.
[24] T. Das, B. Payer, M. Cayouette, W.A. Harris, Neuron 37 (2003) 597–609.
[25] S.H. Wang, Y.Q. Zuo, N. Wang, B. Tong, Pak. J. Med. Sci. 33 (2017) 1328–1332.
[26] F. Helmchen, W. Denk, Nat. Methods 2 (2005) 932–940.
[27] S. Wang, J. Liu, C.C. Goh, L.G. Ng, B. Liu, Adv. Mater. 31 (2019) 1904447.
[28] H.M. Kim, B.R. Cho, Chem. Rev. 115 (2015) 5014–5055.
[29] D. Ding, C.C. Goh, G.X. Feng, et al., Adv. Mater. 25 (2013) 6083–6088.
[30] G.S. He, L.S. Tan, Q.D. Zheng, P.N. Prasad, Chem. Rev. 108 (2008) 1245–1330.
[31] M. Pawlicki, H.A. Collins, R.G. Denning, H.L. Anderson, Angew. Chem. Int. Ed. 48 (2009) 3244–3266.
[32] Z. Zhao, H.K. Zhang, J.W.Y. Lam, B.Z. Tang, Angew. Chem. Int. Ed. 59 (2020) 9888–9907.
[33] X.L. Cai, B. Liu, Angew. Chem. Int. Ed. 59 (2020) 9868–9886.
[34] C. Chen, X. Ni, H.W. Tian, et al., Angew. Chem. Int. Ed. 59 (2020) 10008–10012.
[35] Y.Y. Li, S.J. Liu, H.W. Ni, et al., Angew. Chem. Int. Ed. 59 (2020) 12822–12826.
[36] J. Mei, Y.H. Huang, H. Tian, ACS Appl. Mater. Interfaces 10 (2018) 12217–12261.
[37] J. Shi, Y. Li, Q.Q. Li, Z. Li, ACS Appl. Mater. Interfaces 10 (2018) 12278–12294.
[38] H.D. Li, H.J. Kim, J.J. Han, et al., Aggregate 2 (2021) e51.
[39] M.M. Kang, Z.J. Zhang, N. Song, et al., Aggregate 1 (2020) 80–106.
[40] P.W. Zhou, K.L. Han, Aggregate 3 (2022) e160.
[41] H.F. Su, Q.C. Peng, Y.U. Liu, et al., Biomaterials 288 (2022) 121691.
[42] X.D. Lou, Z.J. Zhao, B.Z. Tang, Small 12 (2016) 6430–6450.
[43] W. Qin, N. Alifu, Y.J. Cai, et al., Chem. Commun. 55 (2019) 5615–5618.
[44] W. Qin, P.F. Zhang, H. Li, et al., Chem. Sci. 9 (2018) 2705–2710.
[45] B.A.D. Neto, P.H.P.R. Carvalho, J.R. Correa, Acc. Chem. Res. 48 (2015) 1560–1569.
[46] W. Qin, K. Li, G.X. Feng, et al., Adv. Funct. Mater. 24 (2014) 635–643.
[47] K. Li, T.B. Ren, S.Y. Huan, L. Yuan, X.B. Zhang, J. Am. Chem. Soc. 143 (2021) 21143–21160.
[48] X.C. Du, H.F. Su, L. Zhao, et al., Mater. Chem. Front. 5 (2021) 7508–7517.
[49] M. Gao, H.F. Su, S.W. Li, et al., Chem. Commun. 53 (2017) 921–924.
[50] D. Wang, H.F. Su, R.T.K. Kwok, et al., Adv. Funct. Mater. 27 (2017) 1704039.
[51] M. Ishikawa, Y. Hashimoto, J. Med. Chem. 54 (2011) 1539–1554.
[52] E. Kim, S. Lee, S.B. Park, Chem. Commun. 48 (2012) 2331–2333.
[53] J. Spandl, D.J. White, J. Peychl, C. Thiele, Traffic 10 (2009) 1579–1584.
[54] J.R. Lakowicz, Introduction to Fluorescence, in: J.R. Lakowicz (Ed.), Principles of Fluorescence Spectroscopy, Springer US, Boston, 2006, pp. 1–26.
[55] G.L. Niu, R.Y. Zhang, Y. Gu, et al., Biomaterials 208 (2019) 72–82.
[56] G.L. Niu, R.Y. Zhang, J.P.C. Kwong, et al., Chem. Mater. 30 (2018) 4778–4787.
[57] A. Amsterdam, R.M. Nissen, Z. Sun, et al., Proc. Natl. Acad. Sci. U. S. A. 101 (2004) 12792–12797.
[58] S.K. Ko, X.Q. Chen, J.Y. Yoon, I. Shin, Chem. Soc. Rev. 40 (2011) 2120–2130.
[59] G.W. Lin, P.N. Manghnani, D. Mao, et al., Adv. Funct. Mater. 27 (2017) 1701418.
[60] D. Fraher, A. Sanigorski, N.A. Mellett, et al., Cell. Rep. 14 (2016) 1317–1329.
[61] J. He, G. Zhang, A.D. Almeida, et al., Neuron 75 (2012) 786–798.
[62] J. Malicki, N. Pooranachandran, A. Nikolaev, X. Fang, A. Avanesov, Methods Cell Biol. 134 (2016) 257–334.
[63] H. Baier, S. Klostermann, T. Trowe, et al., Development 123 (1996) 415–425.
[64] M.G. Honig, R.I. Hume, Trends. Neurosci. 12 (1989) 333–341.
[65] M.G. Honig, R.I. Hume, J. Cell. Biol. 103 (1986) 171–187.
[66] D.I. Danylchuk, P.H. Jouard, A.S. Klymchenko, J. Am. Chem. Soc. 143 (2021) 912–924.
[67] L.F. Guo, M.G. Tian, Z.Y. Zhang, et al., J. Am. Chem. Soc. 143 (2021) 3169–3179.
[68] Y. Tatenaka, H. Kato, M. Ishiyama, et al., Biochemistry 58 (2019) 499–503.
[69] L.F. Guo, M.G. Tian, R.Q. Feng, et al., ACS Appl. Mater. Interfaces 10 (2018) 10706–10717.
[70] R. Matsubara, T. Kaiba, A. Nakata, et al., J. Org. Chem. 84 (2019) 5535–5547.
[71] M. Peng, J.L. Yin, W.Y. Lin, New J. Chem. 42 (2018) 18521–18525.
[72] D. Dang, H.X. Liu, J.G. Wang, et al., Chem. Mater. 30 (2018) 7892–7901.
[73] M. Gao, H.F. Su, Y.H. Lin, et al., Chem. Sci. 8 (2017) 1763–1768.
[74] Y. Yu, H. Xing, H. Park, et al., ACS Mater. Lett. 4 (2022) 159–164.
[75] S.F. Li, W.H. Zhuang, J.R. Chen, et al., Sens. Actuators B: Chem. 346 (2021) 130458.
[76] L. Fan, X.D. Wang, Q. Zan, et al., Anal. Chem. 93 (2021) 8019–8026.
[77] X. Wu, X.X. Wang, Y. Li, et al., Anal. Chem. 94 (2022) 4881–4888.
[78] I.H. Liu, C. Zhang, M.J. Kim, G.J. Cole, Dev. Neurobiol. 68 (2008) 877–898.